# A Theoretical Analysis of Vacuum Arc Thruster Performance *

James E. Polk, Mike Sekerak and John K. Ziemer
Jet Propulsion Laboratory, M/S 125-109, 4800 Oak Grove Drive, Pasadena, CA 91109
(818) 354-9275, james.e.polk@jpl.nasa.gov

Jochen Schein, Niansheng Qi and Robert Binder
Alameda Applied Sciences Corp, 2235 Polvorosa Ave, San Leandro, CA 94577
(510) 483-4156, schein@aasc.net

André Anders
Lawrence Berkeley National Laboratory, 1 Cyclotron Road, Berkeley, CA 94720
(510) 486-6745, aanders@lbl.gov

IEPC-01-211†

**In vacuum arc discharges the current is conducted through vapor evaporated from the cathode surface. In these devices very dense, highly ionized plasmas can be created from any metallic or conducting solid used as the cathode. This paper describes theoretical models of performance for several thruster configurations which use vacuum arc plasma sources. This analysis suggests that thrusters using vacuum arc sources can be operated efficiently with a range of propellant options that gives great flexibility in specific impulse. In addition, the efficiency of plasma production in these devices appears to be largely independent of scale because the metal vapor is ionized within a few microns of the cathode electron emission sites, so this approach is well-suited for micropropulsion.**

## Introduction

Vacuum arcs, or discharges burning in metal vapor liberated from the cathode into an interelectrode gap initially at vacuum, produce high velocity, highly ionized plasma flows which can be exploited for propulsion applications. On cathode surfaces which are too cold to support bulk thermionic emission, current continuity across the metal-vacuum interface is maintained through one or more highly mobile, luminous spots. Although the bulk cathode temperature is relatively low, the local temperature in these spots is well over the boiling point of the cathode material and electrons are emitted by a combination of thermal and field emission. These emission sites are initiated at locations where there are local microprotrusions or dielectric inclusions which cause local enhancement of the applied electric field. Field emission in these regions causes explosive vaporization of the microprotrusion or inclusion due to very rapid Joule heating. A combination of Joule heating and ion bombardment heating sustains the temperatures required to emit electrons and vaporize cathode material. The loss of cathode material causes the formation of a tiny crater on the surface. As the crater diameter grows, the power deposition by ohmic heating and ion bombardment decreases. Eventually the temperature drops to the point where it is no longer possible to sustain electron and vapor emission and the site extinguishes. The characteristic site lifetime appears to be on the order of a few tens of nanoseconds [1, 2, 3, 4, 5]. The resulting craters have a diameter that is typically only 1-10 microns [6, 7], although gross melting may result in larger struc-



†Presented at the 27th International Electric Propulsion Conference, Pasadena, CA, 15-19 October, 2001.

tures [8, 9, 10, 11, 12]. The extinction of an emission site is generally followed by the ignition of a new site at a nearby microprotrusion, often apparently self-generated by the molten metal flows from the previous site. The luminous spot therefore appears to move over the cathode surface.

Extraordinary conditions are achieved in the cathode spots. Current densities on the order of $10^8$ A/cm$^2$ [13, 14] in the emission site and heat fluxes of $10^8$–$10^9$ W/cm$^2$ [15] produce rapid vaporization and ionization of the cathode material. Plasma densities in the near-cathode region reach $10^{20}$–$10^{21}$ cm$^{-3}$ [5, 2], nearly the density of the solid metal. The plasma is generally almost 100 percent ionized, often with multiple charge states [16]. What is truly remarkable is how easy it is to generate these conditions in cold cathode arc discharges. These extreme environments lead to vigorous acceleration of the metal vapor plasma away from the cathode spot, and velocities achieved in the expanding plasma plume are typically on the order of $10^4$ m/s [17, 18].

Vacuum arc-generated plasmas can be used in several different types of propulsion devices. The plasma plumes produced in cathode spots are highly directional, and can be used to produce thrust directly. Vacuum arcs may also be used as plasma sources in ion accelerators such as ion or Hall thrusters. The focus of this paper is on application of vacuum arc discharges in thermal Vacuum Arc Thrusters (VAT's) and in electrostatic Vacuum Arc Ion Thrusters (VAIT's). The unique physical conditions achieved in vacuum arcs offer several potential advantages in these devices. A highly ionized plasma is generated very efficiently in cathode spot operation. Because the ionization process occurs within tens of microns of the emission site, the plasma source is inherently scalable to very small sizes for micropropulsion applications. No magnetic field is required for an efficient discharge, unlike electron bombardment ion engines. Vacuum arc discharges can be operated in pulses with no sacrifice in plasma production efficiency, so the duty cycle can be varied to match the engine power to that available from the spacecraft. This can enable the use of high specific impulse electric thrusters for power-constrained microspacecraft. Finally, because the propellant is provided by the consumable cathode, no gas feed system is necessary. This not only reduces mass and volume, but eliminates the need for low leak-rate valves. It is very difficult to achieve low leak rates in microfabricated valves, so this is a significant advantage over conventional ion engines for microspacecraft applications.

Vacuum arc discharges exhibit certain regularities in their behavior which allow simple, semi-empirical models of thruster performance. The purpose of the models developed in this paper is to provide guidance in choosing cathode materials and explore the performance potential of several implementations of vacuum arc thrusters. We will first describe the performance models and then discuss the performance characteristics of a number of candidate propellants.

## A Semi-Empirical Performance Model

### Vacuum Arc Plasma Sources

Mass is eroded from cathode spots in the form of metal vapor ions, droplets or "macroparticles," and neutral vapor [19, 20, 21], although the majority of the neutral vapor appears to be evaporated from the macroparticles in flight [20, 22]. For sufficiently low values of energy deposited in the cathode, the total erosion rate $\dot{m}_t$ scales with the arc discharge current $J_d$ [23, 24, 25],

$$\dot{m}_t = E_r J_d, \tag{1}$$

The erosion rate $E_r$ is constant in this regime because the mass loss occurs primarily within single, isolated emission sites. Higher current levels are accommodated by more emission sites. Above a certain threshold current or during long pulses the temperature fields of individual emission sites may overlap and cause gross melting. Under these conditions the droplet erosion rate may increase dramatically [26, 27, 28, 29, 30, 31, 32, 33, 34].

The ion component of the mass flux can be described as a current $J_i$, which is the sum of the currents $J_Z$ associated with the fluxes of ions in various charge states $Z$. Experiments over a wide range of conditions show that the ion current in the spot

plasma plume can be expressed as a nearly constant fraction $f_i$ of the discharge current ranging from 0.07 to 0.1 [23, 26, 31]. We can therefore write the ion flow in the cathode spot plasma as

$$J_i = \sum_Z J_Z = f_i J_d \tag{2}$$

and the ion mass flow rate as

$$\dot{m}_i = \sum_Z \frac{J_Z M_i}{Ze} = \frac{f_i J_d M_i}{e} \langle Z^{-1} \rangle, \tag{3}$$

where $e$ is the charge on an electron, $M_i$ is the mass of the ion, $\langle Z^{-1} \rangle$ represents the mean inverse charge state,

$$\langle Z^{-1} \rangle = \sum_Z \frac{f_Z}{Z}. \tag{4}$$

and $f_Z$ is the ratio of the current due to a single charge state to the total ion current,

$$f_Z = \frac{J_Z}{J_i}. \tag{5}$$

This charge state distribution (CSD) is assumed to be constant for a given cathode material. An equilibrium composition of multiply charged ions is created in the hot, high density metal vapor plasma near the emission zone and "freezes" at some point in the plume from the cathode spot as the recombination rate drops due to plasma expansion and cooling [35]. Measurements in pulsed discharges show that the CSD for a certain material changes over the first 100 $\mu$s of the discharge and then becomes relatively constant [36]. The CSD does not vary significantly with discharge current over a range of 50-1200 A [4, 37], but may be influenced by applied magnetic fields and higher discharge currents [38, 39]. The fraction of the total mass loss that occurs in the form of ions is given by the expression

$$F_i = \frac{f_i M_i \langle Z^{-1} \rangle}{e E_r}. \tag{6}$$

The plasma is accelerated to high velocities within a few hundred microns of the cathode spot by gasdynamic (electron pressure gradient and electron-ion friction) forces and possibly by electrostatic forces created by a potential hump that forms above

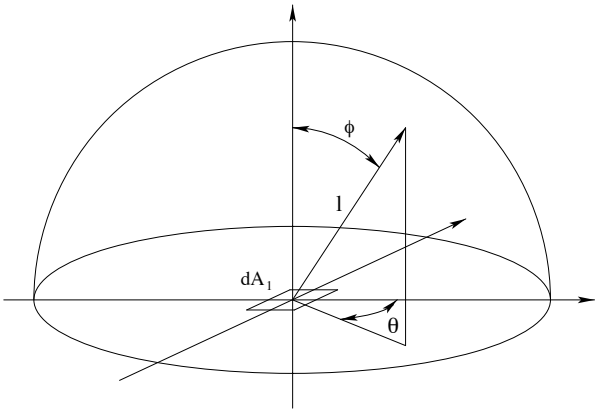


Figure 1: Geometry used to define ion current distribution.

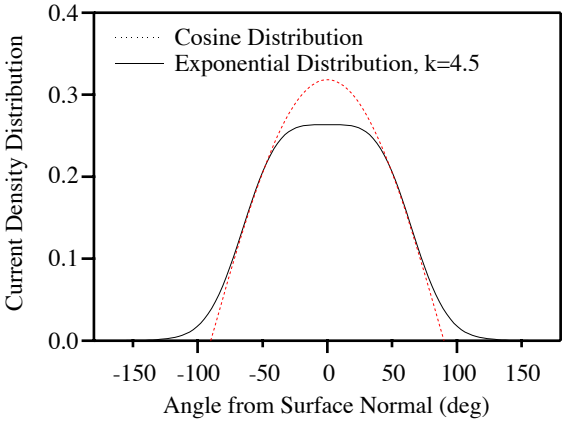


Figure 2: Normalized angular ion current distribution for cosine and exponential functions.

the emission site [40]. Experimental measurements of the ion current density in the plume expanding from the cathode region in vacuum arcs suggest that it follows a cosine [20, 41, 42] or exponential distribution [40]. The geometry used in defining these distributions is shown in Fig. (1). For a cosine distribution in polar coordinates the current density at a radius $l$ and angle $\phi$ defined from the surface normal due to mass generated in area $dA_1$ on the cathode surface is

$$j_{ip}(l, \phi) = \frac{j_{ic} \cos \phi dA_1}{\pi l^2} \tag{7}$$

where $j_{ic}$ is the ion current flux from the cathode surface. This function normalized to a value of $j_{ic} dA_1 = 1$ is plotted in Fig. (2).

The cosine distribution is naturally truncated at

$\phi = 90$ degrees, but ion current is often observed at higher angles [40]. This ion backflow is obviously not generated at the cathode surface but is the result of forces acting on the plasma plume away from the electrode structure. The exponential distribution assumes that the current drops exponentially with the solid angle subtended by the polar angle $\phi$. This distribution often more accurately captures the ion current density at high angles, and as shown in Fig. (2), permits ion current backflow. This distribution is given by

$$j_{ip}(l,\phi) = \frac{2 j_{ic} dA_1}{\sqrt{\pi} l^2 k \,\mathrm{erf}(2\pi/k)} \times \exp(-[2\pi(1-\cos\phi)]^2/k^2), \quad (8)$$

where $k$ is a constant which determines the spread in the distribution. With the assumptions discussed above, the ion current density at the cathode surface can be written as $j_{ic} = f_i j_d$. The ion mass flow rate at the point $(l, \phi)$ due to erosion at $dA_1$ is given by

$$\dot{m}_{ip}(l,\phi) = \frac{M_i j_{ip}}{e} \langle Z^{-1} \rangle. \quad (9)$$

This relationship relies on the assumption that the CSD is independent of angle, so that $j_Z/j_{ip} = f_Z$ everywhere in the plume. Some angular variation in CSD due to electric fields in the plume and charge exchange with neutral atoms evaporated from macroparticles at high angles is observed [43], but these effects are not expected to significantly affect the calculated performance, however.

The ion velocity $u_i$ is assumed to be a constant for all ion charge states of a given material. This is justified by experimental data which generally show that the velocity does not vary significantly with current or angle [18]. A weak variation with charge state is observed [44]. The discharge voltage $V_d$ is also assumed to be constant for a given cathode material. This is also justified by experiment, which shows that the burning voltage for a given material is dominated by the cathode fall [45]. The voltage does vary weakly with anode geometry [46] and significant voltage drops can occur in current leads or the cathode material itself [45].

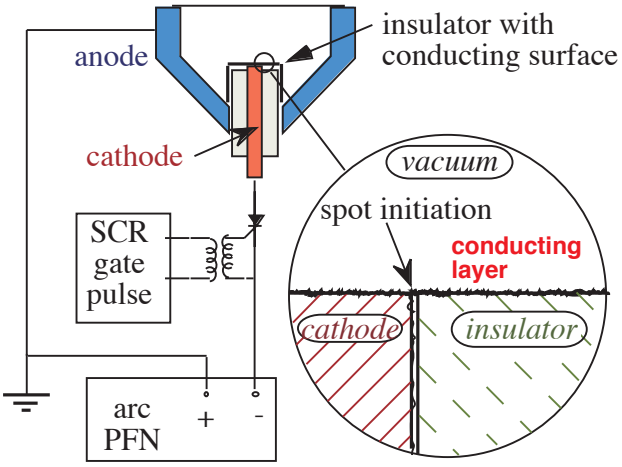


Figure 3: Schematic of a vacuum arc thruster.

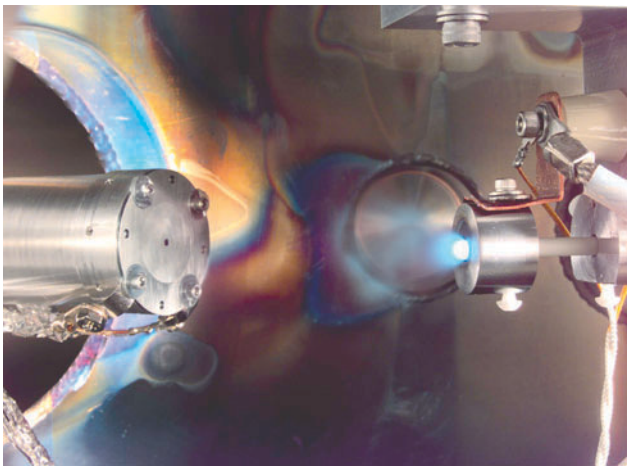

Figure 4: Photograph of a laboratory model vacuum arc thruster.

**Vacuum Arc Thruster Performance**

In the vacuum arc thruster (VAT) the expanding cathode spot plasma is used to produce thrust. The general configuration of a thruster developed by Alameda Applied Sciences Corporation [47] is shown in Fig. (3). Figure (4) shows a photograph of a VAT with a titanium cathode and molybdenum anode that was built and tested at JPL. This design consists of a central rod-shaped cathode separated from a coaxial anode by a thin-walled insulating tube. The face of the cathode and insulator may in general be recessed from the anode face. The consumable cathode rod would have to be fed into the discharge region as material is eroded from it. Inductively or

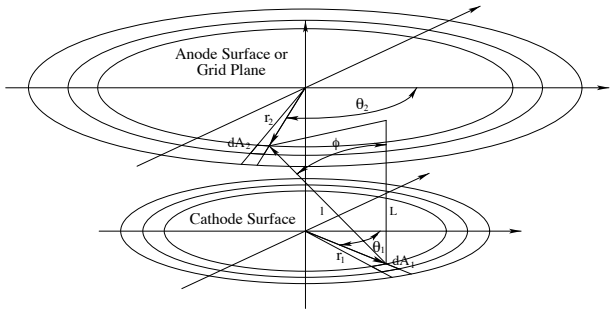


Figure 5: Geometry used to calculate the momentum flux through the anode plane.

capacitively driven pulsed discharges are ignited in this configuration by what is called"triggerless" operation [48]. A thin conducting film on the surface of the insulator produces a high but finite impedence between the cathode and anode. When a relatively low voltage of several hundred volts is applied between the electrodes breakdown occurs at very small gaps or flaws in the thin metal film. These tiny discharges produce enough metal vapor to initiate the main discharge in the gap. Metal vapor and droplets eroded from the cathode replenish the thin conducting layer on the insulator.

The thrust for this configuration can be derived by integrating the momentum flux through the aperture in the anode plane. The geometry used to calculate the thrust is shown in Fig. (5). The differential thrust due to ion flux from area $dA_1$ on the cathode surface through area $dA_2$ at the anode exit plane is given by

$$\begin{aligned} dT &= d\dot{m}_{ip}(l,\phi)(u_i\cos\phi)(cos\phi dA_2) \\ &= \frac{M_i j_{ip}}{e}\langle Z^{-1}\rangle u_i\cos^2\phi dA_2. \end{aligned} \quad (10)$$

Integrating this over the cathode surface and the anode exit plane yields the expression

$$T = \frac{M_i f_i J_d u_i}{e}\langle Z^{-1}\rangle C_t(\overline{L},\overline{r}_a), \quad (11)$$

which represents the thrust that would be achieved if all of the eroded ion flux exited the engine with a velocity $u_i$ directed along the axis multiplied by a thrust correction factor $C_t$ which accounts for plume divergence and deposition of eroded cathode material on the anode interior walls. This expression also assumes that the discharge current density is uniform over the cathode surface, $j_d = J_d/\pi r_c^2$, where $r_c$ is the cathode radius. In any single discharge this assumption is violated because the current is highly nonuniform, concentrated in individual cathode spots. This approach will give the correct average thrust over many discharges if the erosion rate of the cathode is uniform, as it must be in a good thruster design.

The thrust correction factor for a cosine distribution is given by integrating over the cathode source plane to determine the total momentum flux through a point on the anode exit plane and then integrating that result over the anode exit area. This yields

$$C_t = \frac{\overline{L}^3}{\pi^2}\int_0^{2\pi}\int_0^{2\pi}\int_0^{\overline{r}_a}\int_0^1 \frac{\overline{r}_1\overline{r}_2 d\overline{r}_1 d\overline{r}_2 d\theta_1 d\theta_2}{\overline{l}^5}, \quad (12)$$

where $\overline{l} = [\overline{L}^2 + \overline{r}_1^2 + \overline{r}_2^2 - 2\overline{r}_1\overline{r}_2\cos(\theta_1-\theta_2)]^{1/2}$. The thruster geometry parameters are nondimensionalized by the cathode radius, so $\overline{L} = L/r_c$ where L is the cathode length, $\overline{r}_1 = r_1/r_c$ and $\overline{r}_2 = r_2/r_c$, where $r_1$ and $r_2$ are the radii in the cathode and anode planes and $\overline{r}_a = r_a/r_c$, where $r_a$ is the anode exit radius. The angles in the cathode and anode planes are given by $\theta_1$ and $\theta_2$. The corresponding thrust correction factor for the exponential distribution is

$$C_t = \frac{2\overline{L}^2}{\pi^{3/2}k\,\mathrm{erf}(2\pi/k)} I_1 \quad (13)$$

where

$$I_1 = \int_0^{2\pi}\int_0^{2\pi}\int_0^{\overline{r}_a}\int_0^1 \frac{\exp(\frac{-[2\pi(1-\overline{L}/\overline{l})]^2}{k^2})dA_1 dA_2}{\overline{l}^4} \quad (14)$$

and $dA_1 dA_2 = \overline{r}_1\overline{r}_2 d\overline{r}_1 d\overline{r}_2 d\theta_1 d\theta_2$. These integrals were evaluated numerically for a range of electrode goemetry parameters $\overline{L}$ and $\overline{r}_a$ and plotted in Fig. (6). For the exponential distribution a spread factor $k = 4.5$ was chosen, based on measurements made with a copper vacuum arc discharge at 100 A [40]. The maximum thrust is achieved when the anode and cathode surfaces are coplanar, so the anode does not shadow the plasma flux. With this geometry, the thrust coefficient is 0.67 for a cosine distribution and 0.64 for an exponential distribution

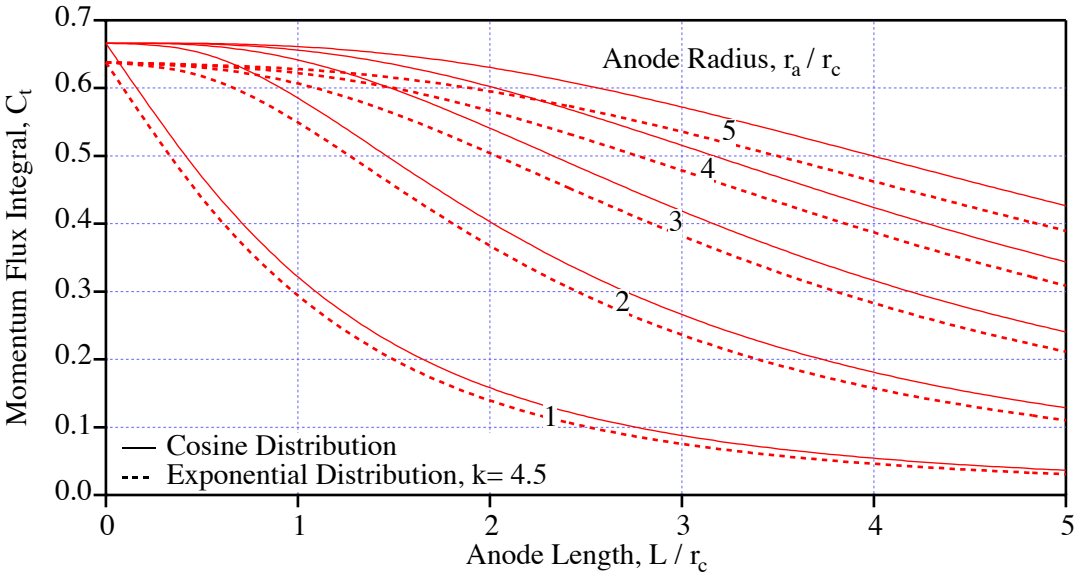


Figure 6: Thrust factor which corrects for plume divergence and loss of plasma to anode walls.

with $k = 4.5$. This maximum thrust coefficient represents the thrust loss due to plume divergence alone.

The specific impulse for a VAT is given by the expression

$$I_{sp} = \frac{T}{\dot{m}_t g} = \frac{M_i f_i u_i C_t}{e E_r g} \langle Z^{-1} \rangle = \frac{F_i u_i C_t}{g}. \quad (15)$$

The power consumed in this simple device is just the discharge power, $P = J_d V_d$. The total efficiency can therefore be expressed as

$$\eta = \frac{T^2}{2\dot{m}_t P} = \frac{M_i^2 f_i^2 u_i^2 C_t^2 (\langle Z^{-1} \rangle)^2}{2e^2 E_r V_d}, \quad (16)$$

and the thrust-to-power ratio is

$$T/P = \frac{M_i f_i u_i C_t}{e V_d} \langle Z^{-1} \rangle. \quad (17)$$

The thrust of a VAT scales with the ion mass $M_i$, ion current fraction $f_i$, plasma velocity $u_i$ and the charge state distribution factor $\langle Z^{-1} \rangle$, which are fundamentally cathode material properties. It also scales with the discharge current $J_d$, which is limited to values greater than the chopping current (the minimum value required to sustain a vacuum arc discharge) and less than the threshold for gross melting. The thrust also depends on the thrust coefficient $C_t$, which argues for an electrode geometry in which the anode does not intercept the cathode spot plasma, such as flush anode and cathode faces. However, other considerations may affect this conclusion. The discharge voltage will depend to some extent on electrode geometry and will likely be higher if the anode surface is not in good contact with the low impedence plasma. Because the droplet flux from the cathode is peaked at high angles (i.e. along the cathode surface) [19, 31, 21], most of the droplets will be captured on the interior anode wall in geometries with a recessed cathode. Some loss in thrust and efficiency may be tolerable if it results in less mass deposition on the spacecraft.

The specific impulse also depends on the material properties and the geometry, but varies inversely with the cathode erosion rate $E_r$. For a fixed ion current fraction $f_i$, a lower total erosion rate implies lower droplet erosion, a mass flux from the consumable cathode which does not contribute significantly to the thrust. The $I_{sp}$ is independent of the discharge current because the plasma acceleration occurs in individual cathode spots for low currents. Increasing the discharge current changes the number of active emission sites, but does not influence the fundamental acceleration mechanism. At higher current levels

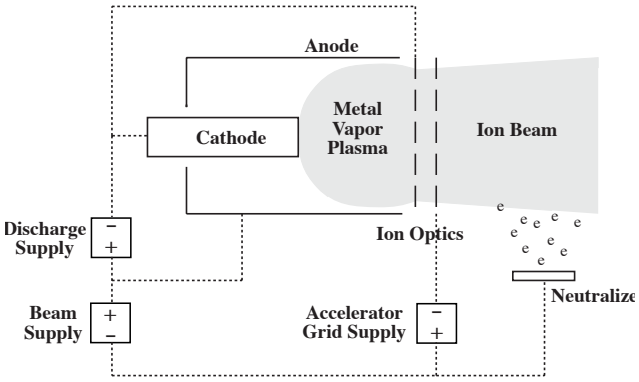


Figure 7: Schematic of a vacuum arc ion thruster.

interactions between spots may lead to additional electromagnetic or electrothermal acceleration, but this will likely occur under conditions which also lead to gross melting and intolerable droplet erosion. The total efficiency scales with the squares of the thrust parameters, inversely with erosion rate and discharge voltage and is independent of discharge current. This underscores the importance of designs which minimize voltage drops in the current leads, cathode structure and interelectrode plasma. For many power-limited micropropulsion applications the thrust-to-power ratio is a critical parameter. To maximize the $T/P$, cathode material with high values of the parameters $M_i$, $f_i$, $u_i$ and low CSDs should be chosen and the electrode geometry should be designed to maximize the parameter $C_t/V_d$.

**Vacuum Arc Ion Thruster Performance**

In Vacuum Arc Ion Thrusters (VAIT's) a device like the VAT is used to supply a plasma which is then accelerated electrostatically with ion optics. A schematic of this implementation with two grid ion optics is shown in Fig. (7), and Fig. (8) shows a photograph of a laboratory model thruster built by JPL and Alameda Applied Sciences Corporation. VAIT's are more complex than the VAT discussed above, but offer much higher performance potential because the ion acceleration process is decoupled from the plasma production.

The operation of the plasma source for the VAIT is assumed to be like that described by the model discussed above. The beam current is given by the fraction of the total arc ion current which is extracted by the ion optics,

$$J_b = f_i J_d C_j \phi_g. \tag{18}$$

The fraction of the total ion current $f_i J_d$ intercepted by the grids is given by the parameter $C_j$ and the fraction of that accelerated through the ion optics is given by the grid transparency $\phi_g$. The current fraction incident on the grids is determined by integrating the current flux from the cathode over the grid area, similar to the procedure used above to determine the momentum flux integral. For a cosine distribution this yields

$$C_j = \frac{\overline{L}^2}{\pi^2} \int_0^{2\pi}\int_0^{2\pi}\int_0^{\overline{r}_g}\int_0^1 \frac{\overline{r}_1\overline{r}_2 d\overline{r}_1 d\overline{r}_2 d\theta_1 d\theta_2}{\overline{l}^4}. \tag{19}$$

For an exponential distribution the optics current is

$$C_j = \frac{2\overline{L}}{\pi^{3/2} k \,\mathrm{erf}(2\pi/k)} I_2 \tag{20}$$

where

$$I_2 = \int_0^{2\pi}\int_0^{2\pi}\int_0^{\overline{r}_g}\int_0^1 \frac{\exp(\frac{-[2\pi(1-\overline{L}/\overline{l})]^2}{k^2}) dA_1 dA_2}{\overline{l}^3}. \tag{21}$$

and, as above, $dA_1 dA_2 = \overline{r}_1\overline{r}_2 d\overline{r}_1 d\overline{r}_2 d\theta_1 d\theta_2$. In these expressions, $L$ is the distance between the cathode and the screen grid, $\overline{L} = L/r_c$, $r_g$ is the radius of the ion optics active beam area and $\overline{r}_g = r_g/r_c$. These integrals are plotted in Fig. (9) for a range of cathode-grid geometry parameters. As with the VAT, these relationships are not valid for a single discharge with a nonuniform distribution of current on the cathode surface, but yield the correct values averaged over many discharges if the cathode erodes uniformly. The grid transparency $\phi_g$ is assumed to be equal to the physical open area fraction of the screen grid. Ion optics with a quiescent upstream plasma typically exhibit an effective transparency greater than the open area fraction because the convex sheath upstream of the screen grid extracts ions from an area larger than the aperture area. In vacuum arc sources the plasma typically approaches the grid with a velocity greater than the Bohm velocity, so

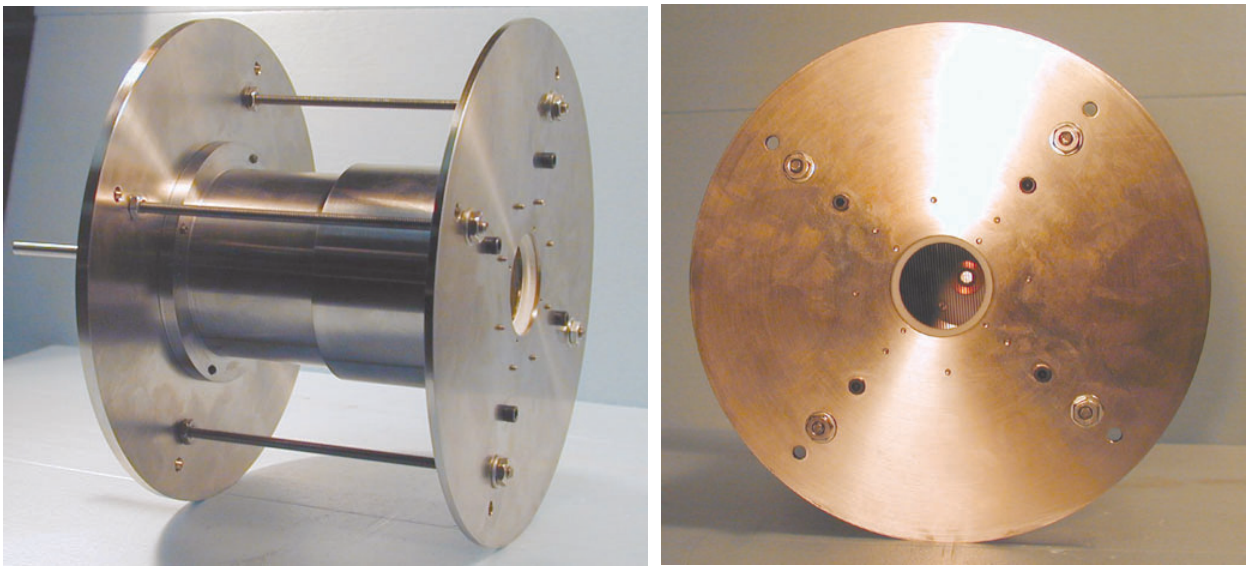

Figure 8: Photograph of a laboratory model vacuum arc ion thruster.

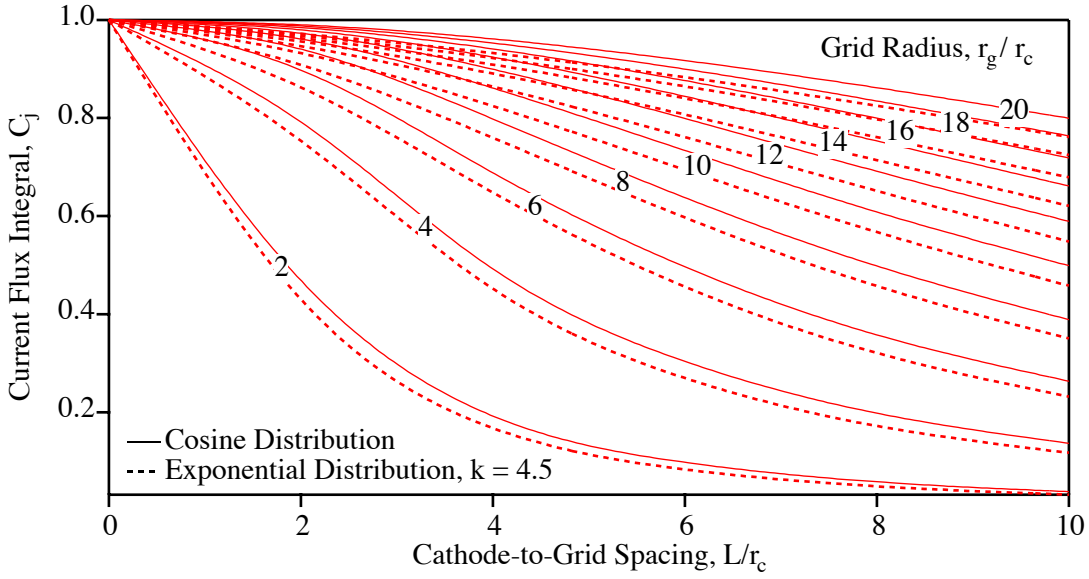


Figure 9: Geometry factor which accounts for ion current to surfaces other than the ion optics.

the ion trajectories will be less affected by the convex equipotential lines near the entrance to the screen grid aperture and the effective transparency will be close to the physical open area fraction.

Equation (18) assumes that the beam current extraction is not limited by optics focusing effects. If we model the ion optics as a plane diode, the maximum ion current density that can be extracted from the upstream plasma is given by the Child-Langmuir law [49],

$$j_b^{max} = \frac{4\epsilon_0}{9\langle Z^{-1/2}\rangle}\left(\frac{2e}{M_i}\right)^{1/2}\frac{V_t^{3/2}}{l_e^2}. \qquad (22)$$

In this expression, $\epsilon_0$ is the permittivity of free space, $l_e$ is the effective gap over which the ions are accelerated, $\langle Z^{-1/2}\rangle = \sum_Z f_Z/Z^{1/2}$, and the total accelerating voltage between the grids $V_t$ is the difference between the beam voltage $V_b$ and the accelerator grid voltage $V_a$. In reality, the current flow between the grids is always at the space charge limit; the plasma boundary (upstream sheath edge) moves, varying the effective acceleration length $l_e$, so that the beam current density given in Eq. (22) is consistent with the flux of ions toward the screen grid aperture. As the upstream plasma flux increases, the plasma boundary moves into the screen grid aperture, and at a certain value of the upstream density the sheath no longer properly focuses the ions through the accelerator grid aperture. This perveance limit for circular apertures is given approximately by Eq. (22) if $l_e = [l_g^2 + d_s^2/4]^{1/2}$, where $l_g$ is the gap between the grids and $d_s$ is the screen grid hole diameter [49]. For a VAIT, the peak ion current density at the screen grid must not exceed the value given by Eq. (22) to avoid direct ion impingement on the accelerator grid. This places a limit on the maximum discharge current (which controls the total plasma production rate and therefore the ion current density) that can be used for a given geometry.

The peak ion current density at the screen grid depends on the distribution of discharge current on the cathode surface and the angular distribution of plasma flowing from the cathode spots. We will consider two limiting cases for each of the angular distributions considered above. The worst case condition occurs when the discharge current is below the spot-splitting current and a single cathode spot carries the entire discharge current. The peak ion current density then occurs directly above this spot. The other limiting case occurs when the discharge current is much higher than the spot splitting current and many spots are simultaneously active. In this limit the discharge current density is approximated as a uniform distribution over the entire cathode surface. The peak ion current density at the screen grid will then occur along the centerline of the thruster. In all cases the peak ion current density at the screen grid is given by an expression of the form,

$$j_{ip}^{max} = \frac{f_i J_d C_j^*(\overline{L})}{\pi r_c^2} \qquad (23)$$

where $C_j^*$ is a geometry factor which depends on $\overline{L}$, the ratio of the distance between the cathode and the grids and the cathode radius.

For a cosine ion current density distribution the geometry parameter for operation with a single spot (low discharge currents) is

$$C_j^* = \frac{1}{\overline{L}^2}. \qquad (24)$$

For operation with many cathode spots (high discharge currents), the peak ion current density at the grids scales with the factor

$$C_j^* = \frac{1}{\overline{L}^2 + 1}. \qquad (25)$$

For an exponential distribution, single spot operation yields a peak ion current density geometry parameter of

$$C_j^* = \frac{2\sqrt{\pi}}{\overline{L}^2 k\,\mathrm{erf}(2\pi/k)}. \qquad (26)$$

For multiple spot operation, the peak ion current density scales with

$$C_j^* = \frac{4\sqrt{\pi}\;\overline{L}}{k\,\mathrm{erf}(2\pi/k)} \times \int_0^1 \frac{\exp(\frac{-[2\pi(1-\overline{L}/\overline{l})]^2}{k^2})\overline{r}_1 d\overline{r}_1}{l^{3/2}}. \qquad (27)$$

Equating these expressions to the space charge-limited current density defined by Eq. (22) and solv-

ing for $J_d$ gives expressions for the maximum discharge current,

$$J_d^{max} = \frac{4\pi r_c^2 \epsilon_0}{9 f_i C_j^* \langle Z^{-1/2} \rangle} \left( \frac{2e}{M_i} \right)^{1/2} \frac{V_t^{3/2}}{l_e^2}. \quad (28)$$

It may be possible to extract more beam current by operating at discharge currents above these limits, but some fraction of the accelerator grid upstream surface will experience direct ion impingement, leading to unacceptably high sputter erosion rates.

The thrust for a given mass flow rate in the beam $\dot{m}_{ib}$ and exhaust velocity $u_e$ is related to the beam voltage $V_b$ by the expression

$$T = \dot{m}_{ib} u_e = \left( \frac{2 M_i V_b}{e} \right)^{1/2} f_i J_d C_j \phi_g \langle Z^{-1/2} \rangle. \quad (29)$$

The maximum thrust is obtained when the source is operated at the maximum discharge current,

$$T_{max} = \frac{16 \pi r_c^2 \epsilon_0 C_j \phi_g V_b^{1/2} V_t^{3/2}}{9 C_j^* l_e^2}. \quad (30)$$

The specific impulse is given by

$$\begin{aligned} I_{sp} &= \frac{f_i C_j \phi_g}{E_r g} \left( \frac{2 M_i V_b}{e} \right)^{1/2} \langle Z^{-1/2} \rangle \\ &= \frac{F_i C_j \phi_g}{g} \left( \frac{2 e V_b}{M_i} \right)^{1/2} \frac{\langle Z^{-1/2} \rangle}{\langle Z^{-1} \rangle} \end{aligned} \quad (31)$$

The total power is assumed to be $P = J_b V_b + J_d V_d$, although this neglects the power required for a neutralizer cathode. With this assumption, the total efficiency can be expressed as

$$\eta = \frac{\eta_u}{(\epsilon_B / V_b + 1)} \frac{\langle Z^{-1/2} \rangle^2}{\langle Z^{-1} \rangle}, \quad (32)$$

where the propellant utilization efficiency is

$$\begin{aligned} \eta_u &= \sum_Z \frac{J_Z M_i C_j \phi_g}{Z e \dot{m}_t} = \frac{M_i f_i C_j \phi_g}{e E_r} \langle Z^{-1} \rangle \\ &= F_i C_j \phi_g \end{aligned} \quad (33)$$

and the beam ion production cost is defined as

$$\epsilon_B = \frac{J_d V_d}{J_b} = \frac{V_d}{f_i C_j \phi_g} \quad (34)$$

Finally, the thrust-to-power ratio can be written as

$$T/P = \frac{(2 M_i V_b / e)^{1/2} \langle Z^{-1/2} \rangle}{V_b / J_d + \epsilon_B} \quad (35)$$

These equations demonstrate what cathode material properties, thruster design parameters and operating conditions influence VAIT performance. The VAIT thrust depends on the material properties $M_i$, $f_i$ and the charge state distribution factor $\langle Z^{-1/2} \rangle$. The dependence on the CSD is somewhat weaker in the VAIT compared to the VAT, which scales with $\langle Z^{-1} \rangle$. The thrust also depends on the engine design through the parameters $C_j$ and $\phi_g$. Maximizing the fraction of ion current captured by the grids drives designs toward close spacing between the cathode and the grids and a large grid radius compared to the cathode radius, as Fig. (9) shows. However, this design approach may exceed the current extraction capabilities of the ion optics. As Eq. (30) shows, the maximum thrust is obtained for the optimum combination of the geometry parameters $r_c^2 C_j \phi_g / C_j^* l_e^2$. There is an interesting tradeoff between the competing parameters $C_j$ and $C_j^*$. The appearance of the grid transparency $\phi_g$ shows that performance scales with open area fraction. In conventional gas discharge ion engines, performance improves with decreasing accelerator grid open area fraction because this helps prevent the loss of neutral propellant atoms. In the VAIT, however, one is not driven to this because there are very few neutrals and those that do exist in the cathode spot plume have a high probability of condensing on the thruster surfaces they contact. The thrust also depends on the operational parameters $J_d$ and $V_b$, as in conventional ion engines.

There is greater flexibility to choose the specific impulse with a VAIT compared to a VAT because the ion velocity depends on the beam voltage, not the cathode spot plasma expansion velocity, as Eq. (31) shows. The $I_{sp}$ also depends on efficient generation of ions with low droplet production through the parameter $F_i$ and effective use of the ion flux through the engine design parameter $C_j \phi_g$.

The total thruster efficiency scales with the propellant efficiency and CSD and inversely with the ratio of beam ion production cost and beam voltage. High propellant efficiency depends on choosing

cathode materials with high ion current fraction and low droplet erosion (high values of $F_i$) and proper accelerator design (high $C_j\phi_g$). Higher efficiency is achieved by using propellants with low average charge states. Clearly the ion production cost must be minimized by choosing materials with a low burning voltage and high ion current fraction and good thruster geometry design. Higher beam voltages can be used to compensate for high ion production costs, although this will increase the $I_{sp}$ and decrease the thrust-to-power ratio for a given discharge current, as Eq. (35) shows.

These relationships suggest the following prescription for designing vacuum arc ion thrusters to meet certain performance specifications. The cathode material must be chosen for high ion current fraction, low droplet erosion rate, low average charge state and good ignition reliability. The beam voltage is determined by the required specific impulse. The ion optics design involves choosing an accelerator grid voltage which prevents electron backstreaming from the neutralizer and a grid spacing which is sufficient to stand off the total accelerating voltage. The grid open area fraction should be maximized, but must satisfy structural and ion beamlet focusing requirements. For operation at the maximum achievable thrust, the geometric parameter $r_c^2 C_j / C_j^*$ must be maximized. Thrust levels lower than the maximum can be obtained by varying the discharge current, and under these conditions the engine performance is optimized by maximizing the parameter $C_j$. The discharge current and duty cycle must be chosen to give the required average thrust level, but must not result in cathode heat inputs which cause gross melting.

## Model Predictions

### Material and Arc Properties

Properties for various potential cathode materials used to estimate the performance of vacuum arc thrusters and vacuum arc ion engines are summarized in Table (1). The current CSDs were calculated from particle charge state distributions and average charge states measured in 100 A pulsed discharges [50]. The CSD was sampled at about 150 $\mu$s after arc initiation; other measurements show that the average charge state is higher for the about the first 100 $\mu$s of a pulsed discharge [36]. The parameters $\langle Z^{-1} \rangle$ and $\langle Z^{-1/2} \rangle$ were calculated from the values of $f_Z$ in the table. Most of the erosion data are from weight loss measurements after sequences of 250 $\mu$s pulses at 100 A [25], although some are from 80–250 A discharges of several seconds duration [23] or 170–300 A arcs of 5 seconds duration [17]. The ion mass fraction $F_i$ was calculated from the erosion rate data assuming an ion current fraction $f_i = 0.1$. As discussed above, this is typically observed in vacuum arc experiments, but is apparently not consistent with some of the erosion rate data. The ion mass fraction for chromium, gadolinium, tantalum and tungsten exceeds unity, suggesting either that the erosion rate measurements are too low or that the ion current fraction is less than 0.1. The impact of this on calculated performance is discussed below. The discharge voltage data are from experiments with 250 $\mu$s pulsed discharges at 300 A [45]. The voltage drops through the leads and the cathode material have been subtracted, so these data represent the arc burning voltage for an anode configuration which is similar to that in VAT's or VAIT's. The ion velocity measurements were sampled from 250 $\mu$s long, 100–200 A discharges [18, 51].

### Predicted Thruster Performance

The equations developed above were used with the material properties for these cathode materials to calculate potential VAT and VAIT performance. The results for the VAT shown in Table 2 assume a discharge current of 10 A and a momentum flux integral $C_t = 0.666$. This is the maximum thrust correction factor for an exponential or cosine distribution, but might be achievable in configurations with the anode and cathode faces flush. The thrust scales linearly with the discharge current, but the other performance parameters are independent of the assumed value. The maximum specific impulse and total efficiency predicted for those species for which we have all the material properties are plotted in Fig. (10). The cathode materials that appear to have the high-

est performance potential in a VAT are magnesium, chromium, yttrium, tantalum and tungsten, with efficiencies ranging from 0.07 to 0.12 and specific impulses of 860 to 1660 s. These materials offer the best performance because of a combination of high ion velocity and high ion fraction. Some of these predictions are artificially high because of the unrealistically high value of ion mass fraction calculated from the experimental erosion rates and an ion current fraction of 0.1. These values are not self-consistent, either because the erosion rates are too low or the ion current fractions are too high. The maximum achievable value of the ion mass fraction is unity, so the effect of increasing the erosion rate or decreasing the ion current fraction to get $F_i = 1$ was explored. As shown in Table 3, this would reduce the specific impulse by 100–200 s and the efficiency by 0.02–0.04. This performance is still competitive with other technologies such as pulsed plasma thrusters that offer very small, controlled impulse bits, and the inherent scalability of vacuum arc-based concepts may provide unique advantages.

The performance predicted for VAIT's is shown in Table 2 and in Fig. (11). For these calculations we assumed a discharge current of 10 A, a beam voltage of 1000 V, a current flux integral $C_j = 0.8$ and a grid open area fraction of 0.8. These values of $C_j$ and $\phi_g$ are high, but probably achievable in a carefully designed engine. As noted above, this approach also neglects the power required for a neutralizer cathode, although this would be justified if a low power neutralizer such as a field emission array cathode were used with the ion source [52]. All of the performance parameters depend on the discharge current or beam voltage, so these results represent a point design which illustrates the impact of cathode material and the performance potential. The best materials appear to be chromium, copper, yttrium, gadolinium, tantalum and tungsten, with efficiencies of 0.42–0.64 and specific impulses at this beam voltage of 4030–7140 s. The impact of varying $f_i$ or $E_r$ to get a realistic upper bound on the ion mass fraction $F_i$ is shown in Table (3). This reduces the specific impulse by 400–1500 s and the efficiency by 0.04–0.2. This suggests that the peak efficiencies for the best materials would be on the order of 0.45 for a beam voltage of 1000 V. The performance could, of course, be improved with higher beam voltages, as Fig. (12) shows. In this figure the total efficiency as a function of specific impulse is plotted for the best cathode materials. The beam voltage ranges from 500 to 5000 V over these curves and for Cr, Gd , Ta and W the ion mass fraction $F_i$ was assumed to be equal to one. As these curves show, the efficiency exceeds 0.5 at specific impulses of 3000 to 9000 s for the different materials. Because the ion generation occurs in a length scale on the order of 10 $\mu$m in the cathode spots, these results are largely independent of the engine size. This therefore appears to be an excellent approach for miniaturizing ion engines. The performance of conventional electron bombardment engines suffers as they are scaled to small sizes because the increased surface-to-volume ratio leads to less efficient plasma production [53].

## Conclusions

The models described in this paper show how the performance of vacuum arc thrusters and vacuum arc ion engines scales with cathode material, engine geometry and operating parameters. These models were used with published values of material properties and optimistic estimates of parameters such as the ion current fraction and the current and momentum flux integrals to determine upper bounds on the performance potential of VAT's and VAIT's. The model results suggest that vacuum arc thruster configurations may be capable of operating at up to 9 percent total efficiency at a specific impulse of 900–1300 s. The advantages of this configuration are that it is very simple, requires no gas feed system, and can be operated with a very simple, low mass power processing unit [47]. The model shows that vacuum arc ion thrusters are capable of much higher performance because the ion acceleration is decoupled from the plasma production process. Efficiencies of 50–60 percent for specific impulses of 3000–9000 s should be achievable in carefully designed engines. This is a very exciting result, because this performance should be largely independent of engine scale. Very small, high performance VAIT's requiring no magnets and no gas feed systems and operating at very low average power levels (in low duty cycle pulsed operation)

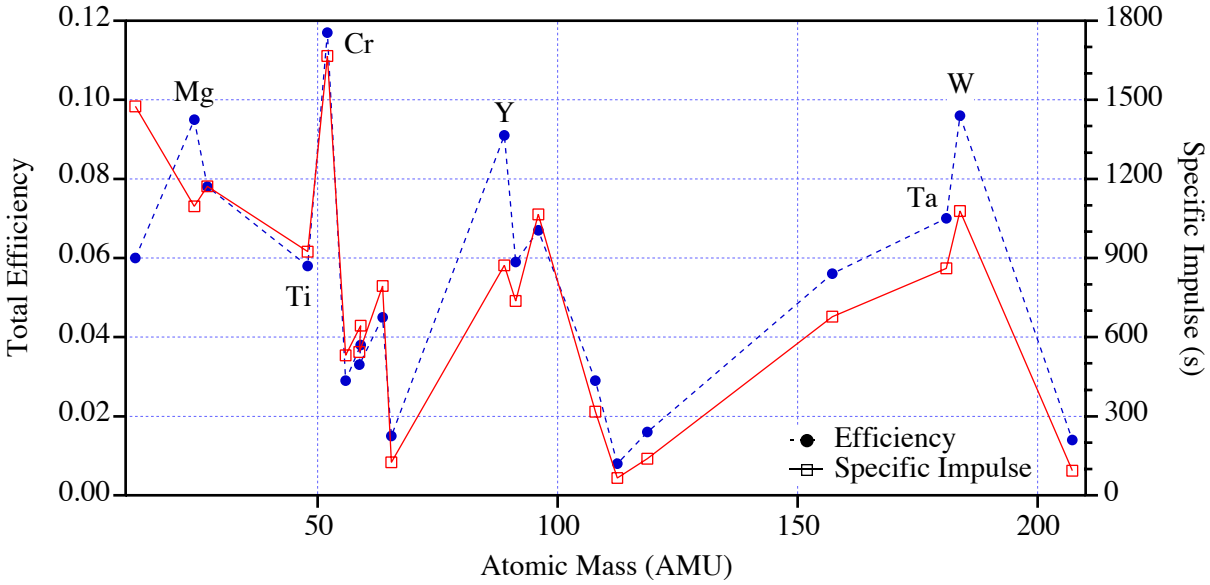


Figure 10: Predicted performance of vacuum arc thrusters for various cathode materials.

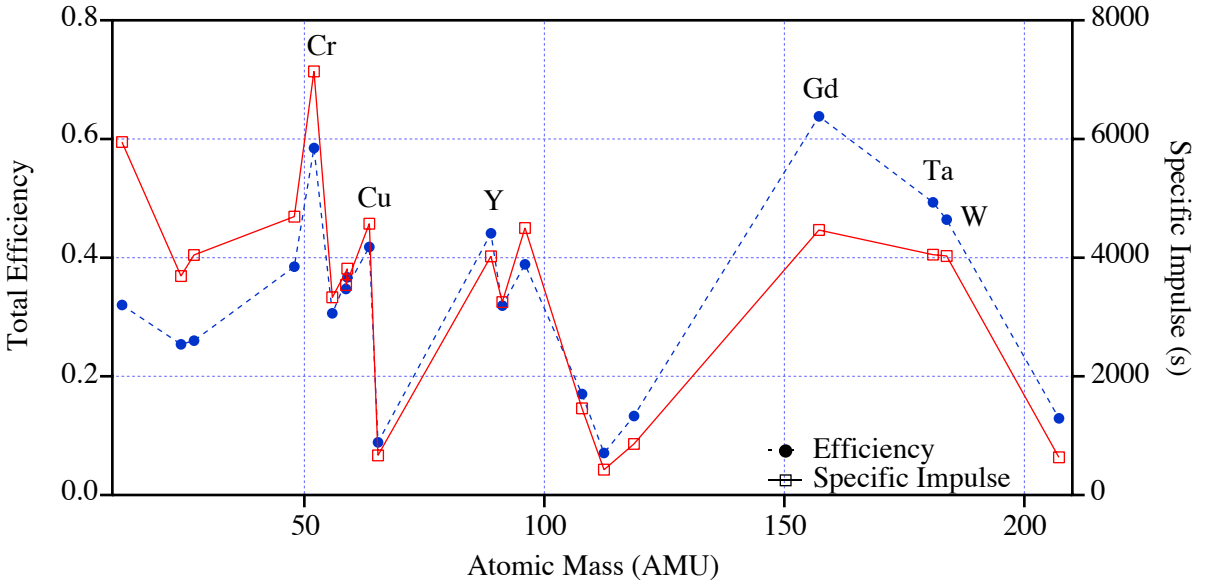


Figure 11: Predicted performance of vacuum arc ion thrusters for various cathode materials.

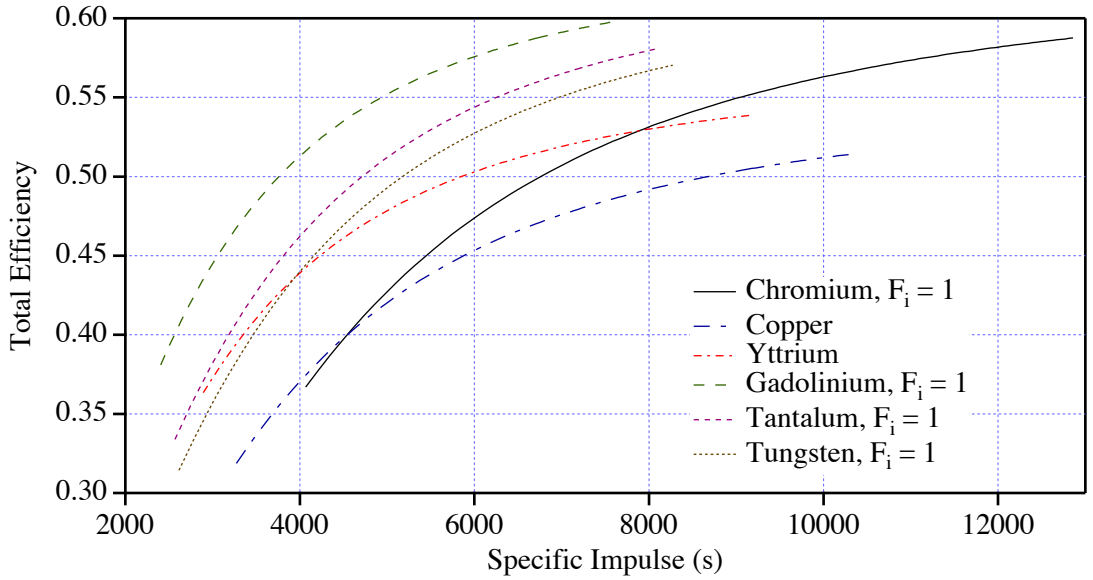


Figure 12: Variation of VAIT efficiency with specific impulse for beam voltages ranging from 500 to 5000 V.

could be an ideal propulsion system for power- and mass-constrained microspacecraft.

Current work is focused on experimentally validating these models with direct thrust and electrical measurements and further characterizing the model input parameters. Preliminary thrust measurements for a VAT with a titanium cathode yielded a thrust-to-power ratio of 2.2 $\mu$N/W [47, 54]. Using the geometry of the thruster and the measured discharge voltage, the model described here predicts a performance of 3.5 $\mu$N/W. This is reasonably good agreement, given the uncertainties in the electrode geometry [47]. Additional thrust measurements using the thruster shown in Fig. (4) with different cathode materials, electrode geometries and discharge currents will be performed to further validate the model. Measurements of the electrical parameters and direct thrust measurements for the VAIT shown in Fig. (8) with various materials, geometries and operating conditions will be used to verify the VAIT model predictions. In addition, vacuum arc plasma sources are being characterized in a special ultra-high vacuum facility. The purpose of these experiments is to verify the model assumptions and measure the model input parameters such as erosion rates, ion current fractions, CSDs, angular ion current density distributions, ion velocities and discharge voltages [55].

Additional engineering challenges will have to be overcome to realize the potential of vacuum arc plasma sources. Arc ignition reliability with the triggerless method is an important issue, although preliminary tests demonstrating up to 1 million discharges are encouraging [48]. Uniform erosion of the cathode must be achieved and a reliable method of dispensing the consumable cathode must be developed. The threat of spacecraft contamination by condensible metal propellants has to be addressed. Finally, adequate engine lifetime must be demonstrated, which will require a thorough understanding of potential failure modes such as insulator and grid erosion and electrical shorts from metal vapor or macroparticle deposition. These are certainly challenging issues, but the predicted performance and scalability of vacuum arc-based thruster concepts indicate that the effort is justified. The unusual conditions achieved in vacuum arc discharges provide unique advantages for advanced propulsion systems.

## Acknowledgements

The research described in this paper was conducted in part at the Jet Propulsion Laboratory, California Institute of Technology, and was sponsored by the National Aeronautics and Space Administration.

## References


[1] B. Jüttner. Characterization of the Cathode Spot. *IEEE Transactions on Plasma Science*, PS-15(5):474–480, 1987.

[2] A. Anders, S. Anders, B. Jüttner, W. Bötticher, H. Lück, and G. Schröder. Pulsed Dye Laser Diagnostics of Vacuum Arc Cathode Spots. *IEEE Transactions on Plasma Science*, 20(4):466–471, 1992.

[3] V.F. Puchkarev, D.I. Proskurovskii, and A.M. Murzakaev. Unsteady Processes in the Cathode Spot of a Vacuum Arc at Currents Near the Threshold. I. Spot on a Macrocrater. *Sov. Phys. - Tech. Phys.*, 32(12):1405–1408, 1987.

[4] A. Anders, S. Anders, B. Jüttner, and I. Brown. Time Dependence of Vacuum Arc Parameters. *IEEE Trans. Plasma Sci.*, PS-21(3):305–311, 1993.

[5] A. Anders, S. Anders, B. Jüttner, and H. Lück. High-Resolution Imaging of Vacuum Arc Cathode Spots. *IEEE Trans. Plasma Sci.*, 24(1):69–70, 1996.

[6] J.E. Daalder. *Cathode Erosion of Metal Vapour Arcs in Vacuum*. PhD thesis, Eindhoven University of Technology, Eindhoven, The Netherlands, 1978.

[7] W.H. Zhao, A. Koch, U.H. Bauder, and R. Behrisch. First Wall Erosion by Arcing. *J. Nuclear Materials*, 128 and 129:613–617, 1984.

[8] S. Anders and A. Anders. On Modes of Arc Cathode Operation. *IEEE Transactions on Plasma Science*, 19(1):20–24, 1991.

[9] D.Y. Fang, A. Nürnberg, U.H. Bauder, and R. Behrisch. Arc Velocity and Erosion for Stainless Steel and Aluminum Cathodes. *J. Nucl. Materials*, 111 and 112:517–521, 1982.

[10] B. Jüttner. On the Variety of Cathode Craters of Vacuum Arcs, and the Influence of the Cathode Temperature. *Physica*, 114C:255–261, 1982.

[11] A.W. Nürnberg, D.Y. Fang, U.H. Bauder, R. Behrisch, and F. Brossa. Temperature Dependence of the Erosion of Al and TiC by Vacuum Arcs in a Magnetic Field. *J. Nucl. Materials*, 103 and 104:305–308, 1981.

[12] D.R. Porto, C.W. Kimblin, and D.T. Tuma. Experimental Observations of Cathode-Spot Surface Phenomena in the Transition from a Vacuum Metal-Vapor Arc to a Nitrogen Arc. *J. Appl. Phys.*, 53(7):4740–4749, 1982.

[13] E. Hantzsche and B. Jüttner. Current Density in Arc Spots. *IEEE Trans. Plasma Sci.*, PS-13(5):230–234, 1985.

[14] S. Anders, B. Jüttner, H. Pursch, and P. Siemroth. Investigations of the Current Density in the Cathode Spot of a Vacuum Arc. *Contrib. Plasma Phys.*, 25(5):467–473, 1985.

[15] J. Prock. Time-Dependent Description of Cathode Crater Formation in Vacuum Arcs. *IEEE Trans. Plasma Sci.*, PS-14(4):482–491, 1986.

[16] I. Brown, B. Feinberg, and J. Galvin. Multiply Stripped Ion Generation in the Metal Vapor Vacuum Arc. *J. Appl. Phys.*, 63(10):4889–4898, 1988.

[17] A. Plyutto, V. Ryzhkov, and A. Kapin. High Speed Plasma Streams in Vacuum Arcs. *Sov. Phys. JETP*, 20(2):328–337, 1965.

[18] G. Yushkov, A. Anders, E. Oks, and I. Brown. Ion Velocities in Vacuum Arc Plasmas. *J. Appl. Phys.*, 88(10):5618–5622, 2000.

[19] J.E. Daalder. Cathode Spots and Vacuum Arcs. *Physica*, 104C:91–106, 1981.

[20] D.T. Tuma, C.L. Chen, and D.K. Davies. Erosion Products from the Cathode Spot Region of a Copper Vacuum Arc. *J. Appl. Phys.*, 49(7):3821–3831, 1978.

[21] J.E. Daalder. Components of Cathode Erosion in Vacuum Arcs. *J. Phys. D: Appl. Phys.*, 9:2379–2395, 1976.

[22] G. Eckhardt. Interpretation of Data on Cathode Erosion and Efflux from Cathode Spots of Vacuum Arcs. *J. Appl Phys.*, 46(8):3282–3285, 1975.

[23] C.W. Kimblin. Erosion and Ionization in the Cathode Spot Regions of Vacuum Arcs. *J. Appl. Phys.*, 44(7):3074–3081, 1973.

[24] R. Behrisch. Surface erosion by electrical arcs. In D.E. Post and R. Behrisch, editors, *Physics of Plasma-Wall Interactions in Controlled Fusion*. Plenum Press, New York, 1984.

[25] I.G. Brown and H. Shiraishi. Cathode Erosion Rates in Vacuum-Arc Discharges. *IEEE Transactions on Plasma Science*, PS-1(1):170–171, 1990.

[26] C.W. Kimblin. Cathode Spot Erosion and Ionization Phenomena in the Transition from Vacuum to Atmospheric Pressure Arcs. *J. Appl. Phys.*, 45(12):5235–5244, 1974.

[27] G.S. Belkin and V. Ya. Kiselev. Influence of Electrode Material on Erosion at High Currents. *Soviet Physics–Technical Physics*, 12(5):702–703, 1967.

[28] G.S. Belkin. Dependence of Electrode Erosion on Heat Flux and Duration of Current Flow. *Soviet Physics–Technical Physics*, 15(7):1167–1170, 1971.

[29] N.A. Khizhnyak, B.G. Safronov, V.L. Vereshchagin, and N.P. Popov. Electrode Erosion in Pulsed Plasma Accelerators. *Soviet Physics–Technical Physics*, 15(11):1828–1831, 1971.

[30] E.W. Gray, J.R. Pharney, and J.A. Augis. Cathodic Contact Erosion Due to Short-Duration Gas Breakdown Arcs. *J. Phys. D: Appl. Phys.*, 5:1068–1076, 1972.

[31] J.E. Daalder. Erosion and the Origin of Charged and Neutral Species in Vacuum Arcs. *J. Phys. D: Appl. Phys.*, 8:1647–1659, 1975.

[32] G.V. Butkevich and G.S. Belkin. *Electrical Erosion of High-Current Contacts and Electrodes*. Energiya, Moscow, 1978. Machine translation from the Foreign Technology Division, WPAFB, OH, FTD-ID(RS)T-0798-86.

[33] A. Watson, A.L. Donaldson, K. Ikuta, and M. Kristiansen. Mechanism of Electrode Surface Damage and Material Removal in High Current Discharges. *IEEE Trans. Mag.*, MAG-22(6):1799–1803, 1986.

[34] A.L. Donaldson, F.M. Lehr, and M. Kristiansen. Performance of in situ Copper Alloys as Electrodes in High Current, High Energy Switches. In *SPIE–Space Structures, Power and Power Conditioning*, volume 871, pages 273–279, 1988.

[35] A. Anders. Ion Charge State Distributions of Vacuum Arc Plasmas: The Origin of Species. *Physical Review E*, 55(1):969–981, 1997.

[36] A. Anders. Ion Charge State Distributions of Pulsed Vacuum Arcs–Interpretation of Their Temporal Development. *IEEE Trans. Plasma Sci.*, PS-26(1):118–119, 1998.

[37] I.G. Brown and J.E. Galvin. Measurements of Vacuum Arc Ion Charge-State Distributions. *IEEE Trans. Plasma Sci.*, 17(5):679–682, 1989.

[38] E. Oks, A. Anders, I. Brown, M. Dickinson, and R. MacGill. Ion Charge State Distributions in High Current Vacuum Arc Plasmas in a Magnetic Field. *IEEE Trans. Plasma Sci.*, PS-24(3):1174–1183, 1996.

[39] A. Anders, G. Yushkov, E. Oks, A. Nikolaev, and I. Brown. Ion Charge State Distributions of Pulsed Vacuum Arc Plasmas in Strong Magnetic Fields. *Rev. Sci. Instrum.*, 69(3):1332–1335, 1998.

[40] J. Kutzner and H.C. Miller. Ion Flux from the Cathode Region of a Vacuum Arc. *IEEE Trans. Plasma Sci.*, 17(5):688–694, 1989.

[41] J. Heberlein and D. Porto. The Interaction of Vacuum Arc Ion Currents with Axial Magnetic Fields. *IEEE Trans. Plasma Sci.*, PS-11(3):152–159, 1983.

[42] Y. Cohen, R. Boxman, and S. Goldsmith. Angular Distribution of Ion Current Emerging from an Aperture Anode in a Vacuum Arc. *IEEE Trans. Plasma Sci.*, PS-17(5):713–716, 1989.

[43] I. Aksenov and V. Khoroshikh. Angular Distributions of Ions in a Plasma Stream of a Steady-State Vacuum Arc. In *18th International Symposium on Discharges and Electrical Insulation in Vacuum*, pages 211–214, Eindhoven, The Netherlands, 1998.

[44] K. Tsuruta, K. Skiya, and G. Watanabe. *IEEE Trans. Plasma Sci.*, 25:603, 1997.

[45] A. Anders, B. Yotsombat, and R. Binder. Correlation Between Cathode Properties, Burning Voltage, and Plasma Parameters of Vacuum Arcs. Technical Report LBNL-47271, Lawrence Berkeley National Laboratory, Berkeley, CA, 2001.

[46] M. Keidar, I. Beilis, R. Boxman, and S. Goldsmith. Voltage of the Vacuum Arc with a Ring Anode in an Axial Magnetic Field. *IEEE Trans. Plasma Sci.*, 25(4):580–585, 1997.

[47] J. Schein, N. Qi, R. Binder, M. Krishnan, J. Ziemer, J. Polk, and A. Anders. Low Mass Vacuum Arc Thruster System for Stationkeeping Missions. In $27^{th}$ *International Electric Propulsion Conference*, Pasadena, CA, 2001. IEPC-01-228.

[48] A. Anders, J. Schein, and N. Qi. *Rev. Sci. Instrum.*, 71:827, 2000.

[49] H.R. Kaufman. Technology of Electron-Bombardment Ion Thrusters. *Advances in Electronics and Electron Physics*, 36:364, 1974.

[50] I.G. Brown and X. Godechot. Vacuum Arc Ion Charge-State Distributions. *IEEE Trans. Plasma Sci.*, 19(5):713–717, 1991.

[51] J. Schein, N. Qi, R. Binder, and M. Krishnan. Vacuum Arc Thruster for Small Satellite Applications: Final Report. Technical Report aasc01TM-22, Alameda Applied Sciences Corporation, San Leandro, CA, 2001.

[52] C.M. Marrese. Performance of Field Emission Cathodes in Xenon Electric Propulsion System Environments. In M. Micci and A. Ketsdever, editors, *Micropropulsion for Small Spacecraft*, chapter 11. American Institute of Aeronautics and Astronautics, Virginia, 2000.

[53] R. Wirz, J. Escobedo, P. Sheehan, J. Polk, C. Marrese, and J. Mueller. Development and Testing of a 3 cm Electron Bombardment Micro-Ion Thruster. In $27^{th}$ *International Electric Propulsion Conference*, Pasadena, CA, 2001. IEPC-01-343.

[54] J. Ziemer. Performance Measurements Using a Sub-Micronewton Resolution Thrust Stand. In $27^{th}$ *International Electric Propulsion Conference*, Pasadena, CA, 2001. IEPC-01-238.

[55] M. Sekerak. Master's thesis, California Institute of Technology, Pasadena, CA, USA, To be published in 2002.

| Species | Mass $M_i$ (AMU) | Ion Charge State Distribution [50] | | | | | | | | Erosion Rate[a] $E_r$ ($\mu$g/C) | Ion Fraction $F_i$ | Discharge Voltage [45] $V_d$ (V) | Ion Velocity[b] $u_i$ (m/s) |
|---|---|---|---|---|---|---|---|---|---|---|---|---|---|
| | | $f_1$ | $f_2$ | $f_3$ | $f_4$ | $f_5$ | $f_6$ | $\langle Z^{-1} \rangle$ | $\langle Z^{-1/2} \rangle$ | | | | |
| Li | 6.941 | 1.000 | | | | | | 1.00 | 1.00 | | | 23.5 | 23800 |
| C | 12 | 1.000 | | | | | | 1.00 | 1.00 | 17[23] | 0.732 | 29.6 | 29700 |
| Mg | 24.305 | 0.307 | 0.701 | | | | | 0.66 | 0.80 | 31 | 0.528 | 18.8 | 30600 |
| Al | 26.981 | 0.224 | 0.590 | 0.191 | | | | 0.58 | 0.75 | 28 | 0.577 | 23.6 | 29900[51] |
| Si | 28.086 | 0.450 | 0.504 | 0.043 | | | | 0.72 | 0.83 | | | 27.5 | 25800 |
| Ca | 40.08 | 0.042 | 0.943 | 0.016 | | | | 0.52 | 0.72 | | | 23.5 | 25900 |
| Sc | 44.96 | 0.150 | 0.749 | 0.101 | | | | 0.56 | 0.74 | | | 19.1 | |
| Ti | 47.9 | 0.052 | 0.739 | 0.207 | | | | 0.49 | 0.69 | 30 | 0.815 | 21.3 | 16700[51] |
| V | 50.94 | 0.038 | 0.664 | 0.280 | 0.019 | | | 0.47 | 0.68 | | | 22.5 | 19300 |
| Cr | 52 | 0.048 | 0.638 | 0.296 | 0.019 | | | 0.47 | 0.68 | 20 | 1.265 | 22.9 | 19400 |
| Mn | 54.94 | 0.327 | 0.658 | 0.020 | | | | 0.66 | 0.80 | | | 22 | 10800 |
| Fe | 55.85 | 0.139 | 0.747 | 0.115 | | | | 0.55 | 0.73 | 48 | 0.663 | 22.7 | 11800 |
| Co | 58.93 | 0.200 | 0.682 | 0.121 | | | | 0.58 | 0.75 | 44 | 0.802 | 22.8 | 11800 |
| Ni | 58.71 | 0.167 | 0.727 | 0.102 | | | | 0.56 | 0.74 | 47 | 0.736 | 20.5 | 10900 |
| Cu | 63.55 | 0.080 | 0.612 | 0.291 | 0.019 | | | 0.49 | 0.69 | 35 | 0.914 | 23.4 | 12800 |
| Zn | 65.38 | 0.667 | 0.333 | | | | | 0.83 | 0.90 | 320[17] | 0.176 | 15.5 | 10400 |
| Ge | 69.74 | 0.429 | 0.571 | | | | | 0.71 | 0.83 | | | 17.5 | 11000 |
| Sr | 87.62 | 0.010 | 0.990 | | | | | 0.50 | 0.71 | | | 18 | |
| Y | 88.91 | 0.022 | 0.544 | 0.434 | | | | 0.44 | 0.66 | 45 | 0.898 | 18.1 | 14300 |
| Zr | 91.22 | 0.004 | 0.364 | 0.523 | 0.109 | | | 0.39 | 0.62 | 53 | 0.691 | 23.4 | 15700 |
| Nb | 92.91 | 0.003 | 0.160 | 0.510 | 0.293 | 0.033 | | 0.33 | 0.57 | | | 27 | 15500 |
| Mo | 95.94 | 0.006 | 0.137 | 0.480 | 0.327 | 0.049 | | 0.33 | 0.57 | 36 | 0.903 | 29.3 | 17400 |
| Pd | 106.4 | 0.121 | 0.713 | 0.144 | 0.021 | | | 0.53 | 0.72 | | | 21.3 | 15700 |
| Ag | 107.87 | 0.062 | 0.570 | 0.350 | 0.019 | | | 0.47 | 0.68 | 140[17] | 0.373 | 23.6 | 12500[51] |
| Cd | 112.41 | 0.523 | 0.485 | | | | | 0.77 | 0.87 | 620[17] | 0.142 | 16 | 6800 |
| In | 114.82 | 0.471 | 0.507 | | | | | 0.73 | 0.83 | | | 17.5 | 5500 |
| Sn | 118.69 | 0.313 | 0.693 | | | | | 0.66 | 0.80 | 295 | 0.273 | 17.5 | 7500 |
| Ba | 137.33 | 0.000 | 1.000 | | | | | 0.50 | 0.71 | | | 18.3 | 6700 |
| La | 138.91 | 0.005 | 0.685 | 0.311 | | | | 0.45 | 0.67 | | | 17.2 | 7000 |
| Ce | 140.12 | 0.014 | 0.787 | 0.199 | | | | 0.47 | 0.69 | | | 17.9 | 7000 |
| Pr | 140.91 | 0.014 | 0.613 | 0.373 | | | | 0.44 | 0.66 | | | 20 | 8700 |
| Nd | 144.24 | | 0.765 | 0.235 | | | | 0.46 | 0.68 | | | 19.7 | |
| Sm | 150.4 | 0.010 | 0.779 | 0.211 | | | | 0.47 | 0.68 | | | 14.6 | 7400 |
| Gd | 157.25 | 0.009 | 0.691 | 0.300 | | | | 0.45 | 0.67 | 55 | 1.347 | 21.6 | 7400 |
| Dy | 162.5 | 0.009 | 0.574 | 0.417 | | | | 0.43 | 0.66 | | | 19.8 | 7400 |
| Ho | 164.93 | 0.009 | 0.574 | 0.417 | | | | 0.43 | 0.66 | | | 20 | 8300 |
| Er | 167.26 | 0.004 | 0.534 | 0.445 | 0.017 | | | 0.42 | 0.65 | | | 19 | 8200 |
| Yb | 173.04 | 0.014 | 0.867 | 0.118 | | | | 0.49 | 0.70 | | | 14.4 | |
| Hf | 178.49 | 0.010 | 0.164 | 0.522 | 0.287 | 0.017 | | 0.34 | 0.58 | | | 24.3 | 9200 |
| Ta | 180.95 | 0.007 | 0.225 | 0.389 | 0.328 | 0.051 | | 0.34 | 0.58 | 56 | 1.143 | 28.7 | 11100[51] |
| W | 183.85 | 0.006 | 0.147 | 0.413 | 0.333 | 0.080 | 0.019 | 0.32 | 0.56 | 55 | 1.111 | 31.9 | 14300[51] |
| Ir | 192.22 | 0.019 | 0.278 | 0.519 | 0.165 | 0.019 | | 0.38 | 0.61 | | | 24.5 | |
| Pt | 195.09 | 0.057 | 0.663 | 0.260 | 0.019 | | | 0.48 | 0.69 | | | 22.5 | 6800 |
| Au | 196.97 | 0.070 | 0.761 | 0.168 | | | | 0.51 | 0.71 | | | 19.7 | 5800 |
| Pb | 207.2 | 0.225 | 0.780 | | | | | 0.62 | 0.78 | 510 | 0.257 | 15.5 | 5400 |
| Bi | 208.98 | 0.692 | 0.291 | | | | | 0.84 | 0.90 | | | 15.6 | 4200 |
| Th | 232.04 | 0.000 | 0.166 | 0.124 | 0.166 | | | 0.17 | 0.27 | | | 23.3 | 9900 |
| U | 231.04 | | 0.075 | 0.547 | 0.377 | | | 0.31 | 0.56 | | | 23.5 | 11400 |

[a] Erosion rates are from reference [25] unless otherwise noted.
[b] Velocities are from reference [18] unless otherwise noted.

Table 1: Material and Arc Properties for Potential Cathode Materials

.

| Species | Mass Flow Rate, $\dot{m}_t$ (mg/s) | Vacuum Arc Thruster | | | | Vacuum Arc Ion Thruster | | | | | |
|---|---|---|---|---|---|---|---|---|---|---|---|
| | | Thrust $T$ (mN) | $I_{sp}$ (s) | Total Efficiency $\eta$ | Thrust-to-Power $T/P$ ($\mu$N/W) | Thrust $T$ (mN) | $I_{sp}$ (s) | Propellant Efficiency $\eta_u$ | Ion Production Cost $\epsilon_B$ (eV/ion) | Total Efficiency $\eta$ | Thrust-to-Power $T/P$ ($\mu$N/W) |
| Li | | 1.14 | | | 0.05 | 7.68 | | | 367 | | 8.77 |
| C | 0.17 | 2.46 | 1475 | 0.060 | 0.08 | 10.09 | 5949 | 0.468 | 463 | 0.320 | 10.78 |
| Mg | 0.31 | 3.33 | 1096 | 0.095 | 17.73 | 11.42 | 3689 | 0.338 | 294 | 0.254 | 13.79 |
| Al | 0.28 | 3.20 | 1172 | 0.078 | 13.64 | 11.30 | 4044 | 0.370 | 369 | 0.260 | 12.90 |
| Si | | 3.60 | | | 0.13 | 11.11 | | | 430 | | 12.14 |
| Ca | | 3.71 | | | 0.15 | 9.56 | | | 367 | | 10.92 |
| Sc | | | | | | 10.92 | | | 298 | | 13.14 |
| Ti | 0.3 | 2.70 | 924 | 0.058 | 12.77 | 14.04 | 4689 | 0.522 | 333 | 0.385 | 16.46 |
| V | | 3.17 | | | 0.13 | 9.72 | | | 352 | | 11.24 |
| Cr | 0.2 | 3.27 | 1666 | 0.117 | 14.28 | 14.26 | 7143 | 0.810 | 358 | 0.585 | 16.41 |
| Mn | | 2.69 | | | 0.12 | 14.21 | | | 344 | | 16.52 |
| Fe | 0.48 | 2.50 | 531 | 0.029 | 11.01 | 15.95 | 3329 | 0.424 | 355 | 0.306 | 18.40 |
| Co | 0.44 | 2.77 | 643 | 0.038 | 12.17 | 16.75 | 3815 | 0.514 | 356 | 0.367 | 19.30 |
| Ni | 0.47 | 2.51 | 544 | 0.033 | 12.24 | 16.61 | 3540 | 0.471 | 320 | 0.347 | 19.65 |
| Cu | 0.35 | 2.73 | 794 | 0.045 | 11.65 | 15.98 | 4575 | 0.585 | 366 | 0.418 | 18.29 |
| Zn | 3.2 | 3.91 | 125 | 0.015 | 0.24 | 21.26 | 666 | 0.113 | 242 | 0.089 | 26.74 |
| Ge | | 3.78 | | | 0.20 | 17.38 | | | 273 | | 21.33 |
| Sr | | | | | | 13.78 | | | 281 | | 16.80 |
| Y | 0.45 | 3.85 | 872 | 0.091 | 21.27 | 18.06 | 4020 | 0.575 | 283 | 0.441 | 21.99 |
| Zr | 0.53 | 3.83 | 737 | 0.059 | 16.38 | 17.20 | 3251 | 0.443 | 366 | 0.319 | 19.68 |
| Nb | | 3.31 | | | 0.12 | 9.36 | | | 422 | | 10.29 |
| Mo | 0.36 | 3.77 | 1066 | 0.067 | 12.85 | 16.16 | 4498 | 0.578 | 458 | 0.389 | 17.32 |
| Pd | | 6.13 | | | 0.28 | 15.99 | | | 333 | | 18.74 |
| Ag | 1.4 | 4.30 | 317 | 0.029 | 0.18 | 20.45 | 1463 | 0.239 | 369 | 0.170 | 23.34 |
| Cd | 6.2 | 4.00 | 66 | 0.008 | 0.24 | 26.51 | 428 | 0.091 | 250 | 0.071 | 33.13 |
| In | | 3.25 | | | 0.18 | 23.30 | | | 273 | | 28.59 |
| Sn | 2.95 | 4.02 | 139 | 0.016 | 22.95 | 25.30 | 859 | 0.174 | 273 | 0.133 | 31.05 |
| Ba | | 3.18 | | | 0.16 | 17.07 | | | 286 | | 20.75 |
| La | | 3.02 | | | 0.17 | 15.47 | | | 269 | | 19.05 |
| Ce | | 3.21 | | | 0.17 | 16.35 | | | 280 | | 19.96 |
| Pr | | 3.76 | | | 0.18 | 15.37 | | | 313 | | 18.30 |
| Nd | | | | | | 16.13 | | | 308 | | 19.27 |
| Sm | | 3.61 | | | 0.23 | 16.78 | | | 228 | | 21.35 |
| Gd | 0.55 | 3.65 | 677 | 0.056 | 16.90 | 24.51 | 4466 | 0.862 | 338 | 0.638 | 28.64 |
| Dy | | 3.61 | | | 0.17 | 16.15 | | | 309 | | 19.27 |
| Ho | | 4.11 | | | 0.20 | 16.27 | | | 313 | | 19.37 |
| Er | | 4.01 | | | 0.20 | 15.97 | | | 297 | | 19.24 |
| Yb | | | | | | 18.69 | | | 225 | | 23.84 |
| Hf | | 3.87 | | | 0.15 | 13.29 | | | 380 | | 15.05 |
| Ta | 0.56 | 4.70 | 861 | 0.070 | 16.49 | 22.64 | 4050 | 0.732 | 448 | 0.493 | 24.42 |
| W | 0.55 | 5.80 | 1078 | 0.096 | 18.24 | 22.12 | 4029 | 0.711 | 498 | 0.464 | 23.06 |
| Ir | | | | | | 15.19 | | | 383 | | 17.16 |
| Pt | | 4.40 | | | 0.19 | 19.57 | | | 352 | | 22.62 |
| Au | | 4.00 | | | 0.19 | 20.76 | | | 308 | | 24.80 |
| Pb | 5.1 | 4.71 | 94 | 0.014 | 30.39 | 32.36 | 636 | 0.164 | 242 | 0.129 | 40.70 |
| Bi | | 5.18 | | | 0.31 | 36.00 | | | 244 | | 45.23 |
| Th | | 2.62 | | | 0.11 | 7.35 | | | 364 | | 8.42 |
| U | | 5.72 | | | 0.23 | 13.93 | | | 367 | | 15.92 |

Table 2: Predicted Performance of Vacuum Arc Thrusters and Vacuum Arc Ion Thrusters

.

| Species | Erosion Rate, $E_r$ ($\mu$g/C) | Ion Current Fraction $f_i$ | Ion Mass Fraction $F_i$ | Vacuum Arc Thruster | | | Vacuum Arc Ion Thruster | | | |
|---|---|---|---|---|---|---|---|---|---|---|
| | | | | $I_{sp}$ (s) | Total Efficiency $\eta$ | Thrust-to-Power $T/P$ ($\mu$N/W) | $I_{sp}$ (s) | Propellant Efficiency $\eta_u$ | Total Efficiency $\eta$ | Thrust-to-Power $T/P$ ($\mu$N/W) |
| Cr | 20 | 0.100 | 1.265 | 1666 | 0.117 | 14.3 | 7143 | 0.81 | 0.585 | 16.4 |
| | 20 | 0.079 | 1.000 | 1316 | 0.073 | 11.3 | 5643 | 0.64 | 0.432 | 15.3 |
| | 25.3 | 0.100 | 1.000 | 1317 | 0.092 | 14.3 | 5647 | 0.64 | 0.462 | 16.4 |
| Gd | 55 | 0.100 | 1.347 | 677 | 0.056 | 16.9 | 4464 | 0.86 | 0.638 | 28.6 |
| | 55 | 0.074 | 1.000 | 501 | 0.031 | 12.5 | 3304 | 0.64 | 0.434 | 26.3 |
| | 74 | 0.100 | 1.000 | 503 | 0.042 | 16.9 | 3319 | 0.64 | 0.474 | 28.6 |
| Ta | 56 | 0.100 | 1.143 | 861 | 0.070 | 16.5 | 4050 | 0.73 | 0.493 | 24.4 |
| | 56 | 0.087 | 1.000 | 749 | 0.053 | 14.4 | 3523 | 0.64 | 0.410 | 23.3 |
| | 64 | 0.100 | 1.000 | 754 | 0.061 | 16.5 | 3544 | 0.64 | 0.432 | 24.4 |
| W | 55 | 0.100 | 1.111 | 1078 | 0.096 | 18.2 | 4029 | 0.71 | 0.464 | 23.1 |
| | 55 | 0.090 | 1.000 | 970 | 0.078 | 16.4 | 3626 | 0.64 | 0.402 | 22.2 |
| | 61 | 0.100 | 1.000 | 972 | 0.087 | 18.2 | 3632 | 0.64 | 0.418 | 23.1 |

Table 3: Effect of decreased ion mass fraction or increased erosion rate on performance.